



U.S. DEPARTMENT OF  
**ENERGY**

PNNL-19719

Prepared for the U.S. Department of Energy  
Under Contract DE-AC05-76RL01830

# Majorana DUSEL R&D Final Report

JE Fast,  
EW Hoppe,  
EE Mintzer,  
CE Aalseth,  
AR Day,  
DC Gerlach,

OT Farmer III  
M Liezers  
EA Lepel  
HS Miley  
DJ Edwards

September 2010



**Pacific Northwest**  
NATIONAL LABORATORY

**DISCLAIMER**

This report was prepared as an account of work sponsored by an agency of the United States Government. Neither the United States Government nor any agency thereof, nor Battelle Memorial Institute, nor any of their employees, makes **any warranty, express or implied, or assumes any legal liability or responsibility for the accuracy, completeness, or usefulness of any information, apparatus, product, or process disclosed, or represents that its use would not infringe privately owned rights.** Reference herein to any specific commercial product, process, or service by trade name, trademark, manufacturer, or otherwise does not necessarily constitute or imply its endorsement, recommendation, or favoring by the United States Government or any agency thereof, or Battelle Memorial Institute. The views and opinions of authors expressed herein do not necessarily state or reflect those of the United States Government or any agency thereof.

PACIFIC NORTHWEST NATIONAL LABORATORY

*operated by*

BATTELLE

*for the*

UNITED STATES DEPARTMENT OF ENERGY

*under Contract DE-AC05-76RL01830*

**Printed in the United States of America**

**Available to DOE and DOE contractors from the  
Office of Scientific and Technical Information,**

**P.O. Box 62, Oak Ridge, TN 37831-0062;**

**ph: (865) 576-8401**

**fax: (865) 576-5728**

**email: [reports@adonis.osti.gov](mailto:reports@adonis.osti.gov)**

**Available to the public from the National Technical Information Service,  
U.S. Department of Commerce, 5285 Port Royal Rd., Springfield, VA 22161**

**ph: (800) 553-6847**

**fax: (703) 605-6900**

**email: [orders@ntis.fedworld.gov](mailto:orders@ntis.fedworld.gov)**

**online ordering: <http://www.ntis.gov/ordering.htm>**

# Majorana DUSEL R&D Final Report

JE Fast,  
EW Hoppe,  
EE Mintzer,  
CE Aalseth,  
AR Day, DJ  
DC Gerlach

OT Farmer III  
M Liezers  
EA Lepel  
HS Miley  
DJ Edwards

September 2010

Prepared for  
the U.S. Department of Energy  
under Contract DE-AC05-76RL01830

Pacific Northwest National Laboratory  
Richland, Washington 99352



## Executive Summary

This report summarizes the work performed at PNNL under the project “Majorana Neutrinoless Double Beta Decay DUSEL R&D” over the period of FY07-FY09. The MAJORANA DEMONSTRATOR experiment requires very low-background components to achieve the sensitivity required to study neutrinoless double-beta decay. There are two classes of materials of primary concern from a radiometric background standpoint. The first is the copper that will form the inner liner of the shield and the major structural components around the detectors, including the vacuum cryostats. The second, and more problematic, is the cabling and other non-copper components (“small parts”) that must reside in close proximity to the detector elements and which can not be significantly shielded.

The first section of this report discusses the cabling and “small parts” for which radiometric background control during manufacturing is problematic. The research effort in this area is further broken into two efforts: 1) obtaining commercial components and performing radiometric assay of those items to screen them for acceptability for use in Majorana and 2) development of a high value (2-10 GOhm) resistor fabricated using silicon-on-sapphire wafers that, in principle, are intrinsically very low background.

The second section of the report discusses developments in the production and assay of ultra-high purity copper. Constituting the majority of the mass of the detector, copper also represents the largest potential contributor to instrument background. As copper of increasing purity is produced, assay limits have been pushed lower, necessitating the concurrent development of improved assay methods. At the same time, it has become increasingly difficult to further purify copper from the impurities of interest, so efforts have also been focused on understanding the mechanisms of contaminant co-deposition. To these ends, an ICP-MS-based method for assay of thorium in ultra-pure copper was developed, and copper nucleation and growth were studied using scanning electron microscopy (SEM) and secondary ion mass spectrometry (SIMS). In addition, a multi-channel electro-analytical potentiostat was acquired to elucidate the electrochemical mechanisms at play during electro-deposition. A portable clean room was also purchased to provide a clean environment for experiments involving very low levels of thorium and uranium.

## Contents

Executive Summary .....	1
1.0 Cables and Small Parts .....	4
1.1 Radioassay of commercial products.....	4
1.1.1 Assay Method and Results .....	4
1.1.2 Assay Conclusion.....	17
1.2 Silicon-on-Sapphire Resistors .....	17
2.0 Ultra-High Purity Copper Production and Assay .....	18
2.1 Development of ICP-MS Assay Methods.....	18
2.1.1 Introduction .....	18
Methods and Results .....	19
Discussion and Conclusions.....	20
2.2 Radiometric Assay .....	21
Introduction.....	21
2.2.1 Methods and Results .....	21
2.3 Nucleation and Growth Studies, other Assay Techniques .....	22
2.3.1 Introduction.....	22
Methods and Results .....	22
Discussion and Conclusions.....	28
2.4 Conclusions .....	28
3.0 References .....	29

## Figures and Tables

Figure 1: Marinelli used to count wire. Note black electrical tape used to hold cable in place in initial counting. This tape was subsequently counted alone to see if the tape was a significant contribution to the cable assay results.....	5
Figure 2: Plot of 58704-43A bare wire. Blue is sample spectrum, green is background spectrum. ....	7
Figure 3: 58704-43A minus background.....	7
Figure 4: 58704-43B wire with shield. Blue is the sample spectrum, green is the background spectrum. ....	8
Figure 5: 58704-43B wire with shield minus background.....	8
Figure 6: 58704-43C bare wire after cleaning. Blue is the sample spectrum, green is the background spectrum.....	9
Figure 7: 58704-43C bare wire after cleaning minus background.....	9
Figure 8: Spectrum of sample 58704-43D wire ends and tape. Blue is sample spectrum, green is background spectrum. ....	10
Figure 9: Spectrum from wire ends and tap, background subtracted.....	10
Figure 10: Spectrum of 58704—53A ceramic pieces - blue is the sample spectrum, green is the background spectrum. ....	11
Figure 11: Spectrum of ceramic pieces, background subtracted.....	11
Figure 12: Spectrum of sample 58704-53B HV feed through - blue is the sample spectrum, green is the background spectrum.....	12
Figure 13: Spectrum from HV feed throughs, background subtracted.....	12
Figure 14: Picture of High Purity Intrinsic Germanium detector (detector “B”) in its copper-lined commercial lead cave.....	13
Figure 15: High voltage feed throughs.....	14
Figure 16: SOS resistor structure. Total device size is 1.2 mm x 2.0 mm and the measured resistance is 9-11 GOhm at room temperature.....	18
Table 1: Gamma Energy Results for Majorana Small Parts Assay – wire (Activity in Bq/Kg).....	15
Table 2. HV Feed-thru and ceramic substrate Assay Results.....	16
Table 3: <sup>232</sup> Th normalized to μBq/kg Cu from blanks using TRU resin.....	19
Table 4: <sup>232</sup> Th (μBq/kg Cu) in Cu samples using TRU resin sample preparation.....	20

## 1.0 Cables and Small Parts

### 1.1 Radioassay of commercial products

Materials of interest for use in the construction of the MAJORANA DEMONSTRATOR detectors have been counted for their gamma-ray emitting radionuclides. Six samples have been counted. Four samples are associated with micro-coax cabling that could be used to carry signals from the detector elements to the front end circuit located within the cryostats and from those circuits out through the cross arm tube to the vacuum feedthroughs located outside the shield. Ceramic pieces representative of substrates for thick film resistors were also counted. These were counted primarily as a comparison to the alternative silicon-on-sapphire design discussed below. Finally, samples of high voltage (HV) feedthroughs were measured. The materials were counted in bulk to allow the measurement of a lower detection limit.

#### 1.1.1 Assay Method and Results

Four samples have been counted in the 329 Low-level Count Room at PNNL. They are:

1. Cooner “Special” wire (32 AWG solid center conductor, FEP insulation, 42 AWG ground braid with Ni/Au, no jacket) referred to as “bare wire” below.
2. Cooner wire CW2040-3275F (32 AWG stranded center, FEP insulation, 42 AWG ground braid with Ni/Au, FEP jacket). Referred to as “wire with jacket” below.
3. Thunderline Z HV feedthroughs (p/n TL-1951)
4. Alumina ceramic

These samples were analyzed in the following six counting runs:

58704-43A bare wire, no jacket, cleaned, weight ~ 1444 g  
 58704-43B wire with jacket, cleaned, weight ~1598.5 g  
 58704-43C recount of -43A after additional cleaning and removal of wire ends and tape, weight ~1443 g  
 58704-43D wire ends and tape, weight ~0.82 g  
 58704-53A ceramic pieces, weight 22.5086 g  
 58704-53B HV feedthroughs, weight 295.51 g, 198 units

The wire was wound around the center protrusion of a 4 L Marinelli beaker (Figure 1). For sample 58704-43A, the wire was wound to a height of 6.7 cm. The wire was just above the top of the center protrusion. No wire was directly above the center protrusion. For sample 58704-43B, the wire was wound to a height of 10.5 cm, approximately 3.8 cm above the center protrusion. Again no wire was placed directly above the center protrusion. For sample 58704-43C, the wire was placed in roughly the same spot as for 58704-43A.

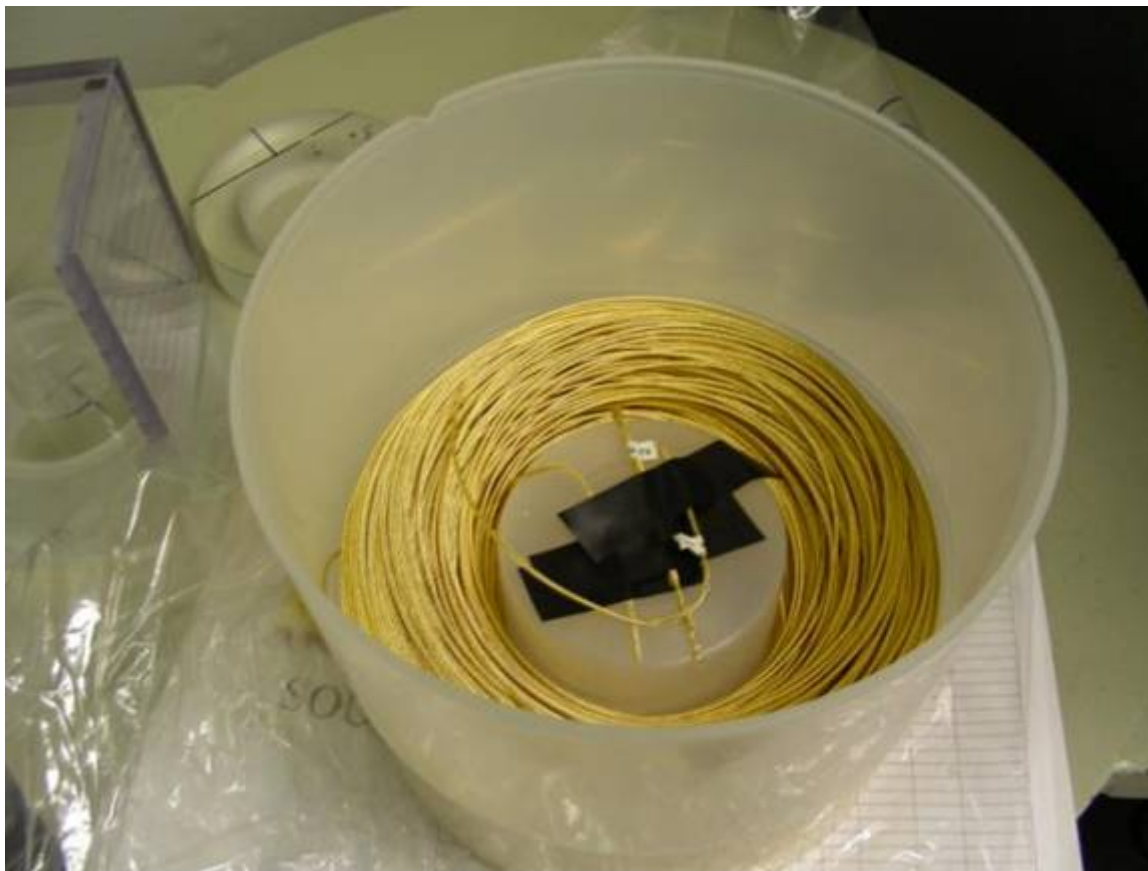


**Figure 1: Marinelli used to count wire. Note black electrical tape used to hold cable in place in initial counting. This tape was subsequently counted alone to see if the tape was a significant contribution to the cable assay results.**

The wire ends and tape from sample 58704-43A were sealed in a poly bag and laid flat on a piece of 1/16" thick Plexiglas placed on top of the face of the high-purity germanium (HPGe) detector for counting.

An average geometry was determined for the two samples; 58704-43A and -43B, which was water at a midpoint between the heights of the wires counted in the 4-L Marinelli beakers. The solution was spiked with the 10-isotope mixed isotope standard obtained from AEA Technology, QSA to allow efficiency calibration of this geometry. Sample 58704-43D was approximated using the geometry of 50 ml in a 9 oz jar counted on the face of a detector.

The ceramic pieces were placed in a small bag which was placed on top of the detector face and counted. Similarly, the HV feedthroughs were also placed in a bag and placed on the top of the detector face.

The samples were counted for approximately five to six days each.

The wire samples and ceramic pieces were counted on detector 6, "B," which is an Ortec low-background detector with a detector volume of 214 cm<sup>3</sup>, relative efficiency of 40%, and a FWHM resolution of 1.90 keV for the 1332.5 keV line of Co-60.

The HV feedthroughs were counted on detector 1, "C," which is an Ortec pop-top detector with a detector volume of 234 cm<sup>3</sup>, relative efficiency of 50%, and a FWHM resolution of 1.95 keV for the 1332.5 keV line Co-60.

Figures 2 and 3 are spectra of sample 58704-43A, which is bare wire. Figure 2 shows the sample spectra with the background spectrum in green. Figure 3 shows the residual spectrum after the background spectrum has been subtracted from the sample spectrum.

Figures 4 and 5 are spectra of sample 58704-43B. Figure 4 shows the sample spectra with the background spectrum in green. Figure 5 shows the residual spectrum after the background spectrum has been subtracted from the sample spectrum.

Figures 6 and 7 are spectra of sample 58704-43C. Figure 6 shows the sample spectra with the background spectrum in green. Figure 7 shows the residual spectrum after the background spectrum has been subtracted from the sample spectrum.

Figures 8 and 9 are spectra of sample 58704-43D. Figure 8 shows the sample spectra with the background spectrum in green. Figure 9 shows the residual spectrum after the background spectrum has been subtracted from the sample spectrum.

Figure 10 and 11 are spectra of sample 58704-53A. Figure 10 shows the sample spectra with the background spectrum in green. Figure 11 shows the residual spectrum after the background spectrum has been subtracted from the sample spectrum.

Figure 12 and 13 are spectra of sample 58704-53B. Figure 12 shows the sample spectra with the background spectrum in green. Figure 13 shows the residual spectrum after the background spectrum has been subtracted from the sample spectrum. Note the large single energy peak for K-40 and the backscatter peak just below the single energy peak.

Figure 14 is a picture of the High Purity Germanium detector in a commercial lead cave with a copper liner.

Figure 15 is a picture of the high voltage feedthroughs.

The gamma-ray energy results for the wire samples are tabulated in Table 1. Before cleaning of the bare wire and removal of the tape, there were measureable quantities of <sup>40</sup>K (280 ± 207 mBq/kg), uranium (~68 ± 10 mBq/Kg), and thorium (~136 mBq/Kg). After cleaning, <sup>40</sup>K was <220 mBq/Kg, uranium (at 253 mBq/Kg), and thorium at ~98 mBq/Kg. The observed radioactivity in these cables makes them unsuitable for Majorana. It was not unexpected that commercially produced wire would not be adequate, but the availability of a commercial product that met the requirements would have been advantageous compared to developing cable production technology in-house.

In the ceramic pieces, there were measurable quantities of uranium daughters (~196 mBq/Kg) but upper limits for the thorium daughters (<62 mBq/Kg). The high level of U reinforces the concern about the use of thick film resistors and motivates development of an alternative path to production of the high value resistors needed in the resistive feedback loop for the detectors.

The HV feedthroughs had <sup>40</sup>K measureable at 330,000 mBq/Kg but barely detectable amounts of uranium daughters and thorium daughters. Since these components would be outside the thick detector shielding the main concern is radon emanation, so the <sup>40</sup>K content is not a significant issue, while the non-detect of U and Th is very encouraging.

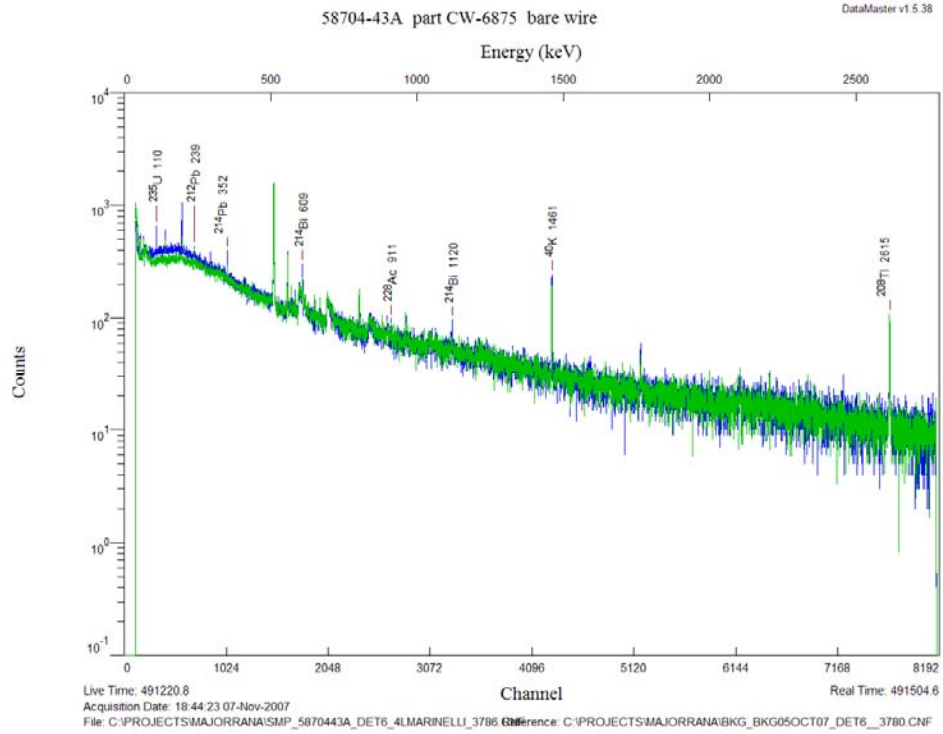


Figure 2: Plot of 58704-43A bare wire. Blue is sample spectrum, green is background spectrum.

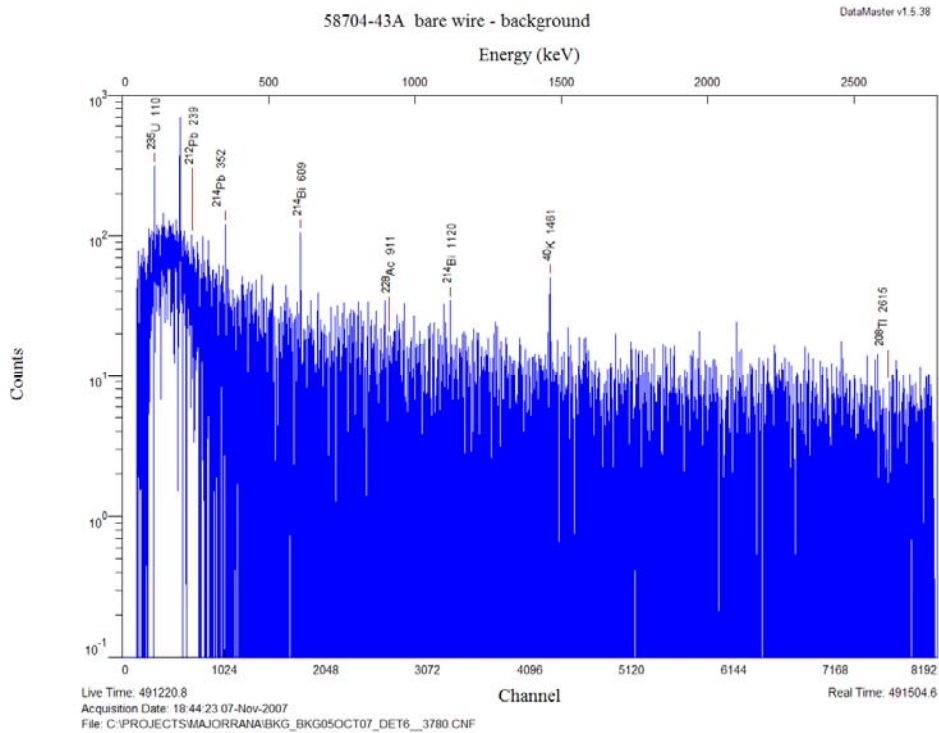


Figure 3: 58704-43A minus background

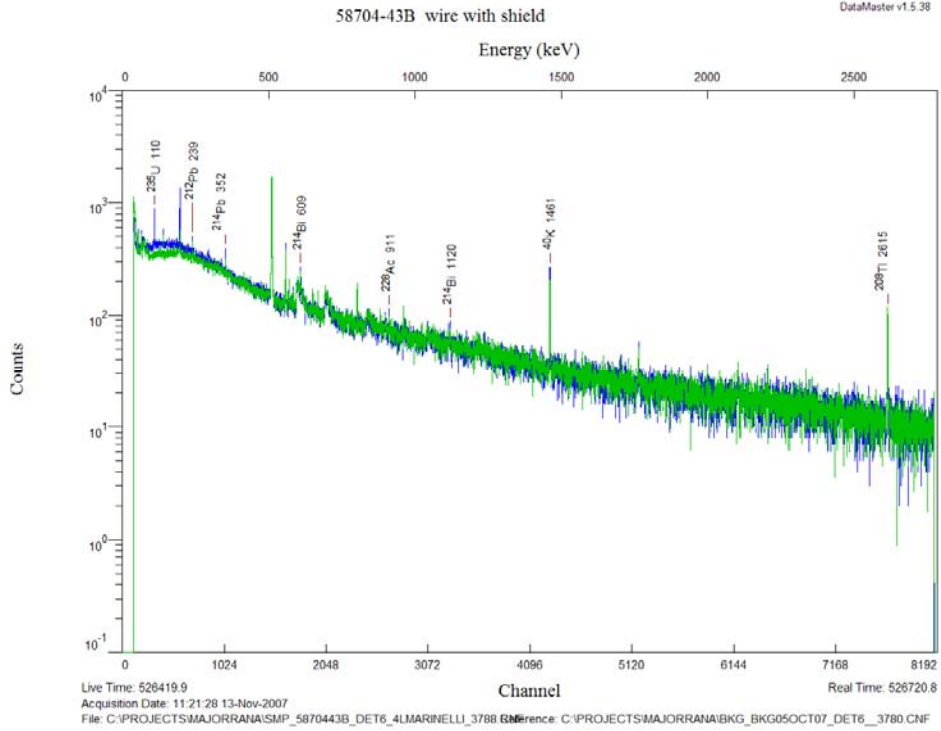


Figure 4: 58704-43B wire with shield. Blue is the sample spectrum, green is the background spectrum.

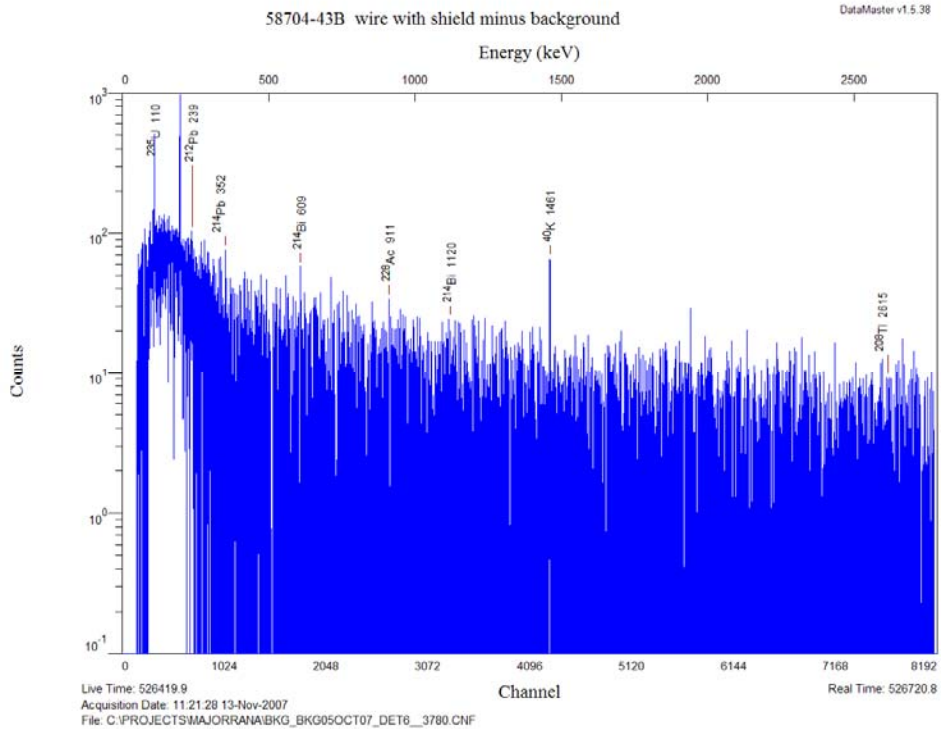


Figure 5: 58704-43B wire with shield minus background

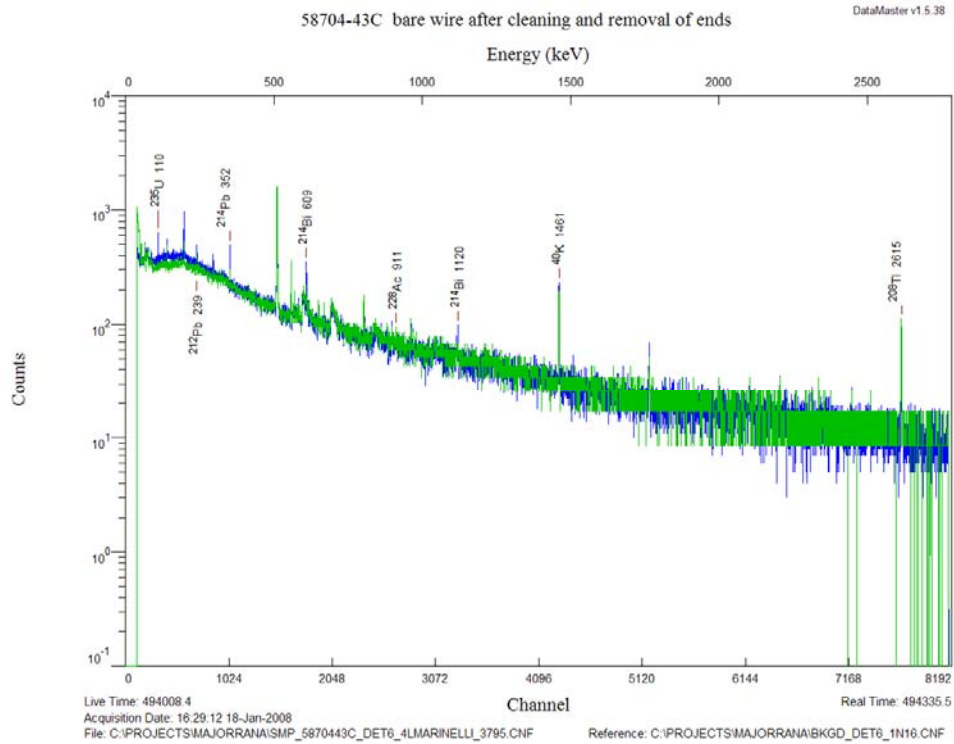


Figure 6: **58704-43C bare wire after cleaning. Blue is the sample spectrum, green is the background spectrum.**

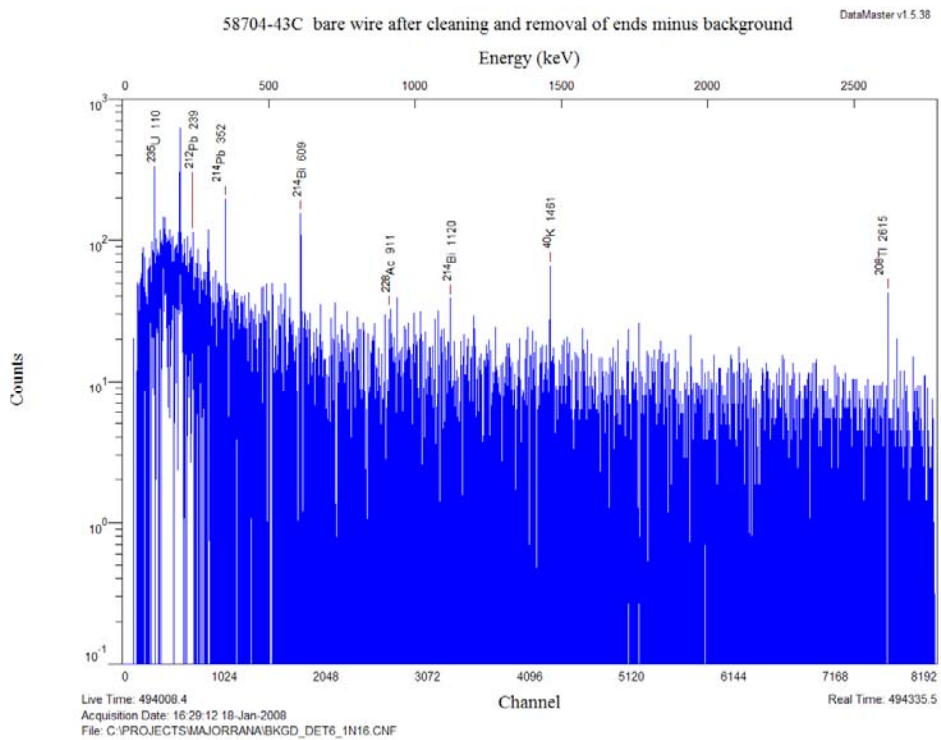


Figure 7: **58704-43C bare wire after cleaning minus background**

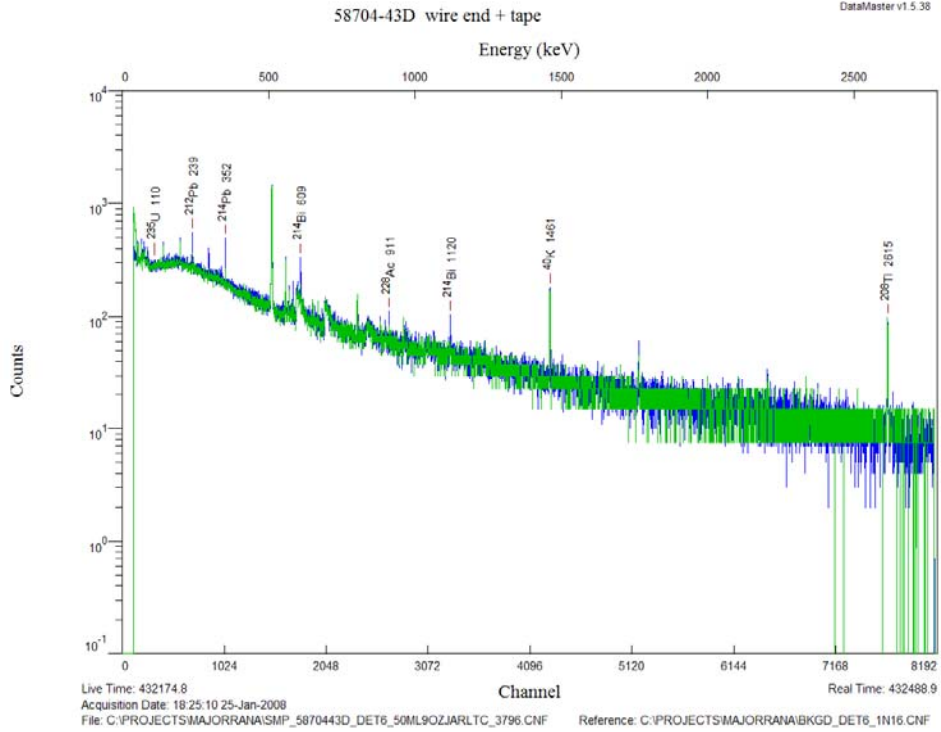


Figure 8: Spectrum of sample 58704-43D wire ends and tape. Blue is sample spectrum, green is background spectrum.

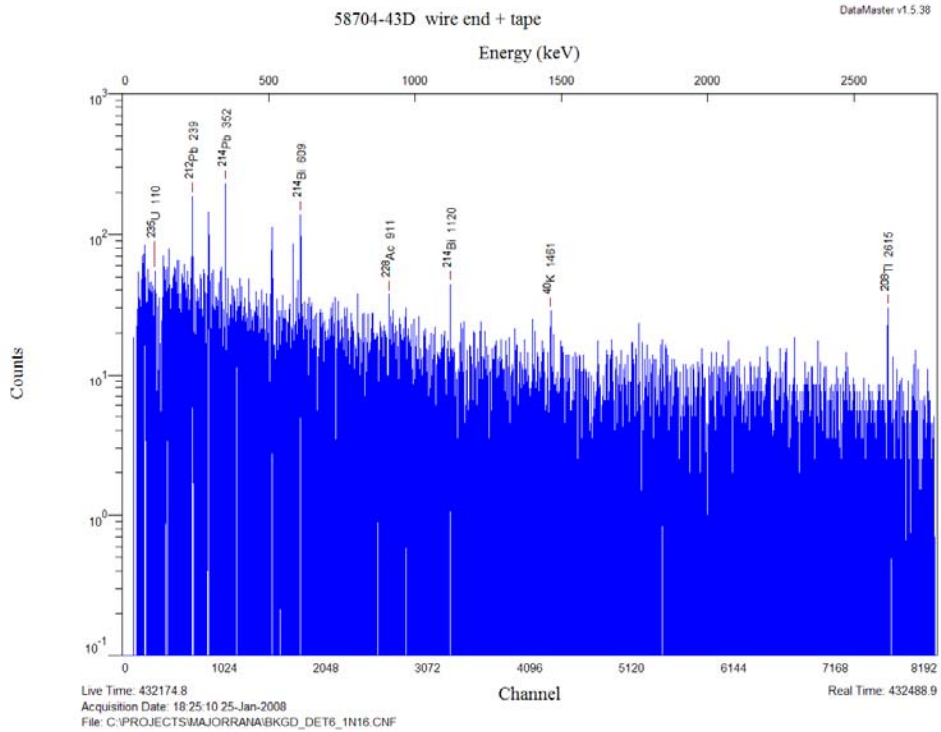


Figure 9: Spectrum from wire ends and tap, background subtracted

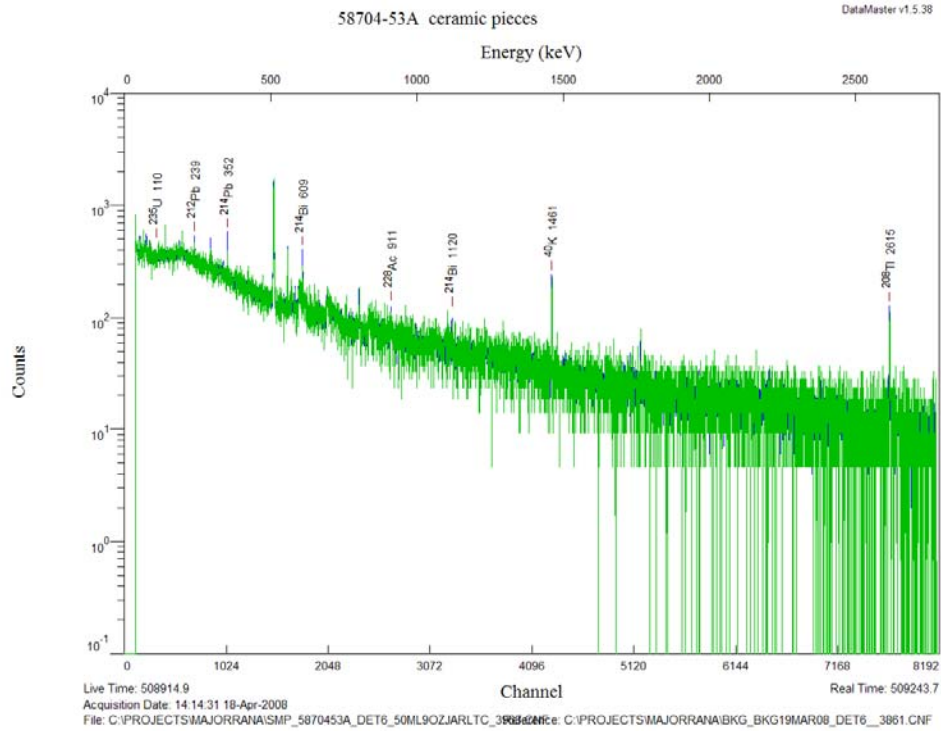


Figure 10: Spectrum of 58704—53A ceramic pieces - blue is the sample spectrum, green is the background spectrum.

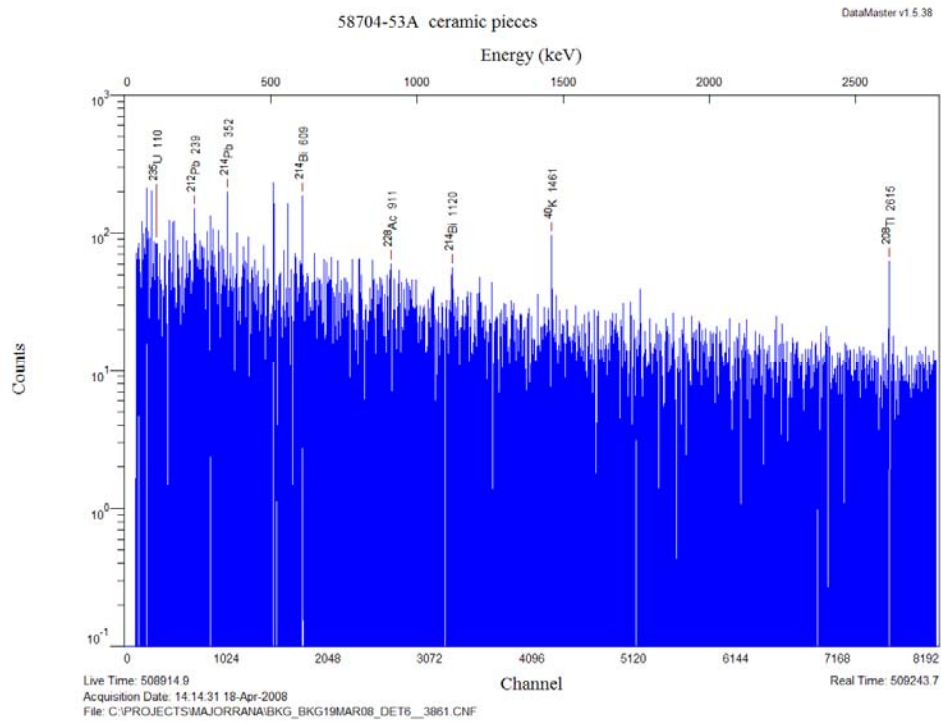


Figure 11: Spectrum of ceramic pieces, background subtracted

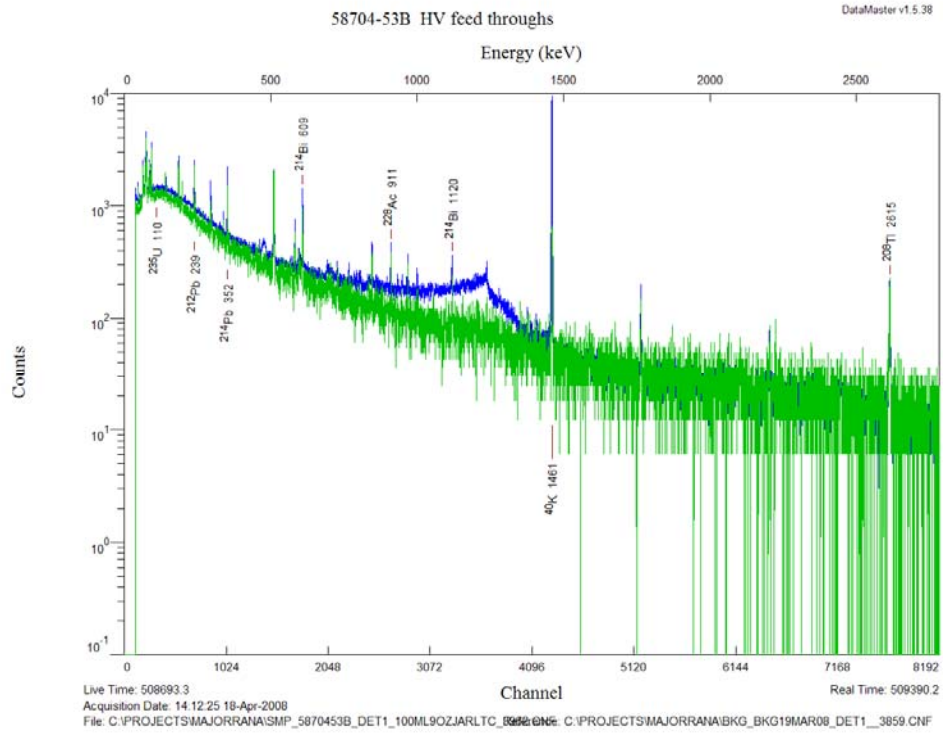


Figure 12: Spectrum of sample 58704-53B HV feed through - blue is the sample spectrum, green is the background spectrum

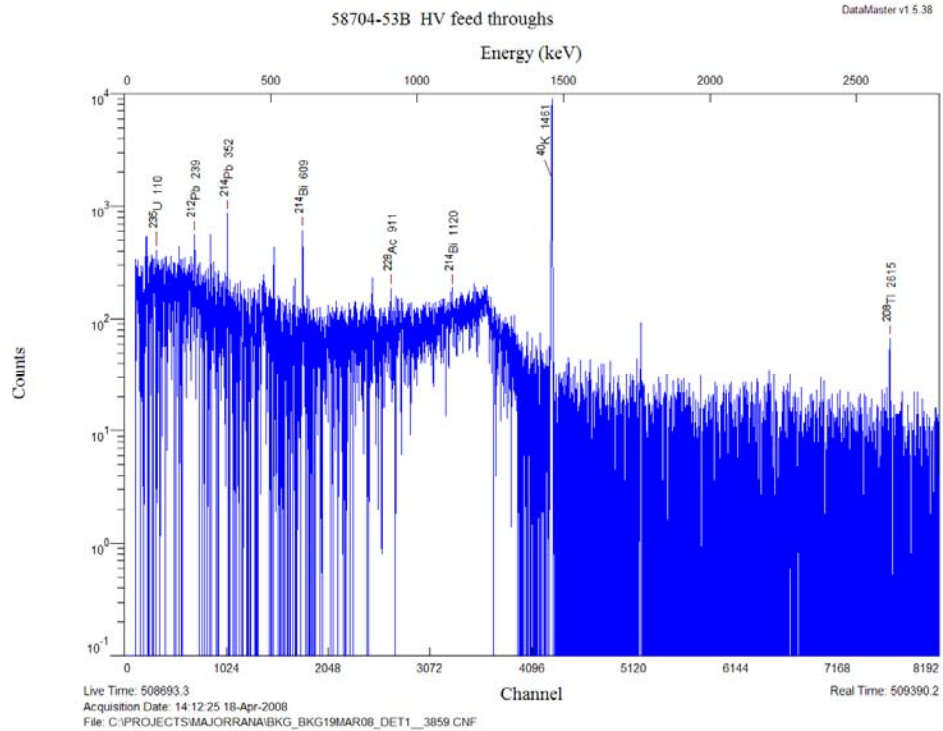
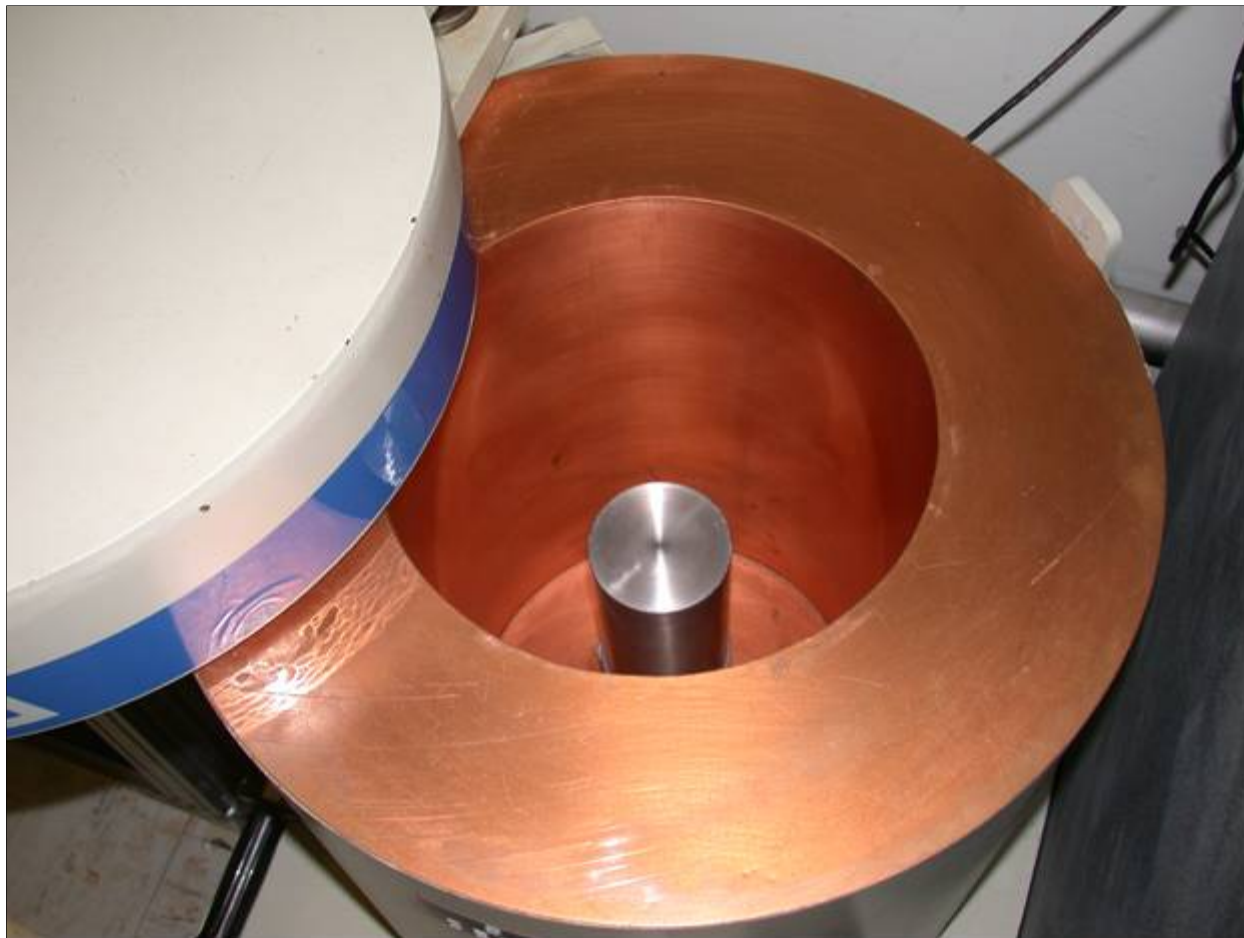


Figure 13: Spectrum from HV feed throughs, background subtracted



**Figure 14: Picture of High Purity Intrinsic Germanium detector (detector "B") in its copper-lined commercial lead cave**

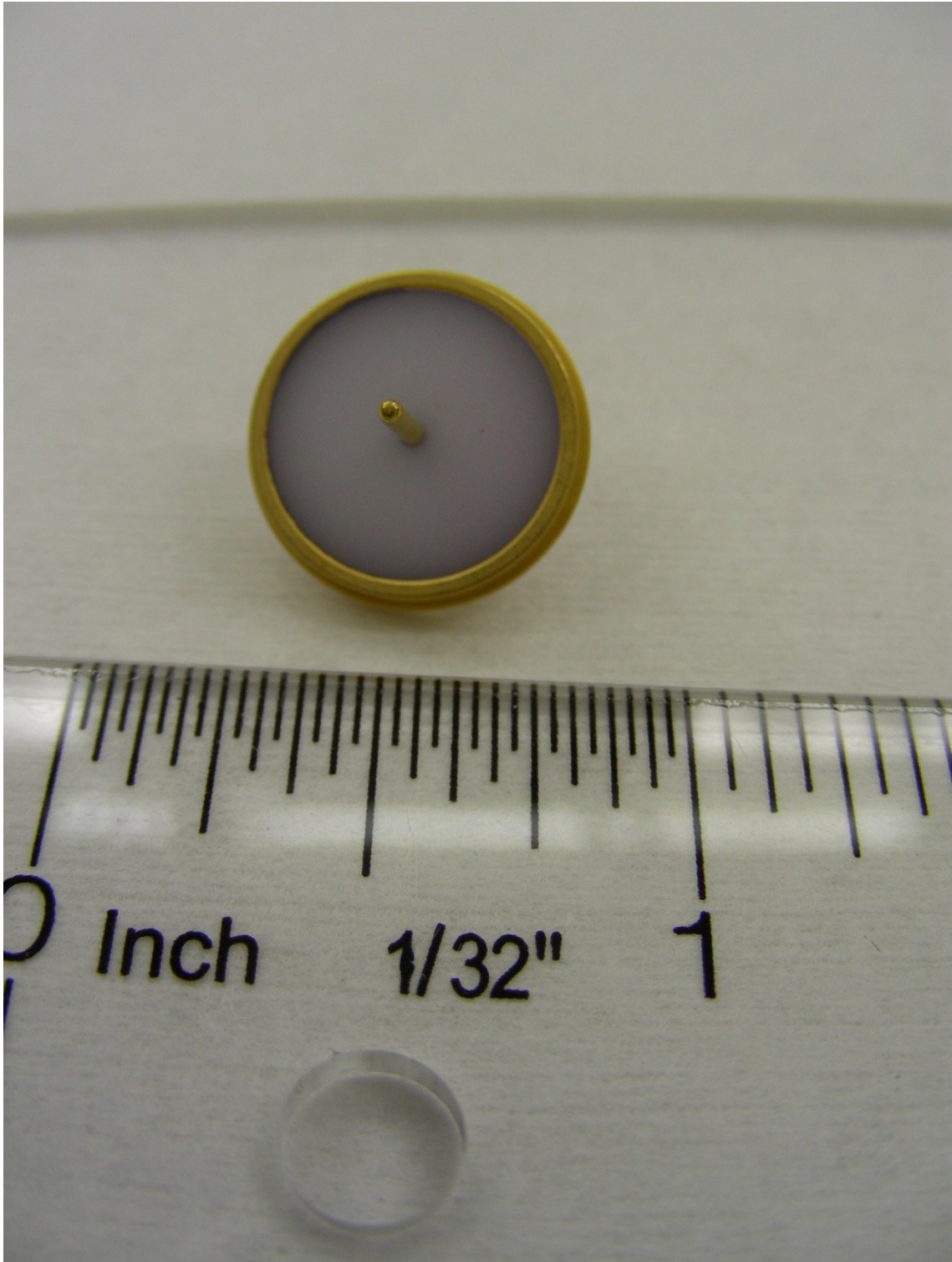


Figure 15: **High voltage feed throughs**

Table 1: **Gamma Energy Results for Majorana Small Parts Assay – wire (Activity in Bq/Kg)**

Activity in mBq/Kg			U-238 chain			
Sample ID	Mass (g)	Live Time (s)	K-40 (1460.75 keV)	Pb-214 (352 keV)	Bi-214 (609 keV)	Pa-234m (1001 keV)
58704-43B wire w shield	1598.5	526420	525 ± 192	60 ± 23	66 ± 25	<2,294
58704-43A bare wire	1444.0	491221	280 ± 207	79 ± 27	215 ± 31	<2,664
58704-43C bare wire after cleaning and removal of ends	1443.0	494008	<218	201 ± 27	305 ± 27	<2,627
58704-43D wire end + tape	0.8	432175	<262,700 <149 mBq/1440g	235,690 ± 25,900 134±15 mBq/1440g	251,600 ± 29,970 143±17 mBq/1440g	<3,126,500 <1,775 mBq/1440g

Activity in mBq/Kg			Th-232 chain			
Sample ID	Mass (g)	Live Time (s)	Pb-212 (238.6 keV)	Bi-212 (727 keV)	Ac-228 (911 keV)	Tl-208 (2614.5 keV)
58704-43B wire w shield	1598.5	526420	<44	<377	177 ± 45	<174
58704-43A bare wire	1444.0	491221	<50	<437	96 ± 30	<200
58704-43C bare wire after cleaning and removal of ends	1443.0	494008	111 ± 26	618 ± 141	85 ± 31	<107
58704-43D wire end + tape	0.8	432175	144,670 ± 17,390 82±10 mBq/1440g	<384,800 <219 mBq/1440g	134,310 ± 36,852 76±21 mBq/1440g	<88,800 <50 mBq/1440g

Report prepared by: Elwood Lepel

2/25/2008

Table 2. HV Feed-thru and ceramic substrate Assay Results

Activity in mBq/Kg			U-238 chain			
Sample ID	Mass (g)	Live Time (s)	K-40 (1460.75 keV)	Pb-214 (352 keV)	Bi-214 (609 keV)	Pa-234m (1001 keV)
58704-53B HV feed throughs (198)		508693	330,040 ± 7,030	1,047 ± 181	<189	<12,210
58704-53A ceramic pieces		508915	<8,510	6,771 ± 1,295	7,696 ± 1,443	<107,300

Activity in mBq/Kg			Th-232 chain			
Sample ID	Mass (g)	Live Time (s)	Pb-212 (238.6 keV)	Bi-212 (727 keV)	Ac-228 (911 keV)	Tl-208 (2614.5 keV)
58704-53B HV feed throughs (198)	0.0	508693	477 ± 155	<1,369	<444	566 ± 274
58704-53A ceramic pieces	0.0	508915	<1,332	<13,320	<3,589	<2,886

Report prepared by: Elwood Lepel 2/25/2008

### 1.1.2 Assay Conclusion

Requirements on coax cables and front-end parts such as thick film resistors (alumina substrates) are most stringent at 10  $\mu\text{Bq/kg}$  U/Th or less. Observed levels are 3-4 orders of magnitude larger, but consistent with observed activity in the tape used to hold the wire in sample holder. However, the wire counted without tape but after the unsuccessful “cleaning” procedure had comparable levels of U/Th. This suggests that this wire is most likely far from clean enough for Majorana use. As a result of this and other relevant published results, Majorana is pursuing in-house fabrication of wiring for the most critical wire runs nearest the detectors.

The HV feedthroughs will be located outside the lead shield and hence the main issue will be radon emanation into the vacuum. The below MDA results for U/Th make these viable candidates for Majorana worthy of further study. The high  $^{40}\text{K}$  level should be simulated to evaluate the impact on the lower energy spectrum for  $2\nu\beta\beta$ , Single Site Time Correlation cuts and dark matter analyses. A direct radon emanation measurement is also required to certify these parts for use.

## 1.2 Silicon-on-Sapphire Resistors

One of the principle components of concern to Majorana is the feedback resistor on the front end circuit that must sit very near the detectors. The only other surface mount component on that circuit is a FET. The FET is mounted as a bare die and wire bonded; hence it is primarily silicon, with a small amount of aluminum metallization. In contrast, the only commercial high value (several GOhm) resistors are of the thick film type. These suffer from high radiometric backgrounds both from the substrate (alumina) and the thick film inks used to create the resistor and contact pads. While resistors of this type were adequate for the IGEX experiment, they are not for Majorana and other current generation experiments. The EXO collaboration is looking into the idea of replacing the alumina substrate with sapphire as the growth of the sapphire crystal is a process that inherently rejects U/Th from the material. They have assayed both sapphire substrates and the inks used in the thick film processing and have found that, while the inks are quite radioactive, they are acceptable for their purposes due to the very small quantity on each device. This is not the case for Majorana where the background constraints are considerably more stringent.

As an alternative, we have developed a silicon-on-sapphire (SOS) resistor with entirely dry processing. We begin with commercially available SOS wafers that have a thin epitaxial silicon layer with a resistivity  $>100$  Ohm-cm and laser ablate the silicon to leave a serpentine resistor structure. Pads at the ends of the device are then metalized (gold) for wire bond connections. The structure is shown in Figure 16. The structure was designed to result in a resistance of 2 GOhm assuming the silicon has a resistivity at the lower limit of 100 Ohm-cm. The measured resistance value for initial articles is 9-11 GOhm at room temperature. This is near the upper end of the range of values one would want for Majorana (lower values are needed as detector leakage current increases). We also anticipate that the resistance will increase as these are cooled to operating temperature (120-150 K). The initial devices have been sent to the University of Washington collaborators to measure the resistance vs. temperature curve. Five 4” wafers have been processed by the vendor, Quik-Pak (formerly Aguila), producing more than enough parts for the full Majorana experiment. Should a lower resistance design be required, it is a straightforward change to the laser ablation programming and would result in reduction of the component size as well. While this has been shown to be a viable path, Majorana is currently pursuing the next level of integration - directly depositing an amorphous germanium resistor on to the front-end board and thus eliminating the need to mount the resistor component and wire bond it to the circuit board.

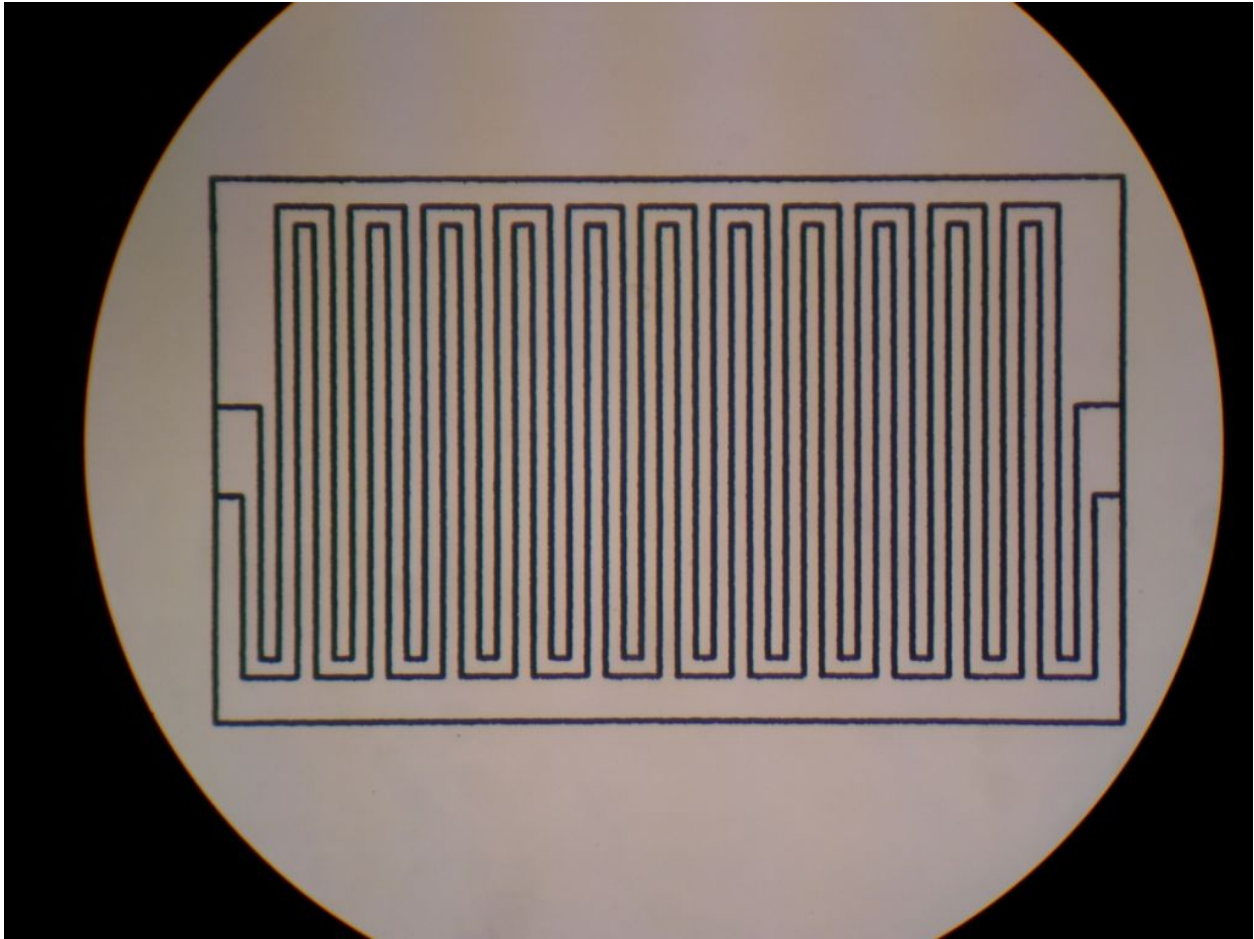


Figure 16: SOS resistor structure. Total device size is 1.2 mm x 2.0 mm and the measured resistance is 9-11 GOhm at room temperature.

## 2.0 Ultra-High Purity Copper Production and Assay

### 2.1 Development of ICP-MS Assay Methods

#### 2.1.1 Introduction

The next generation of nuclear and particle physics experiments, such as the MAJORANA DEMONSTRATOR experiment, require cryostats and shielding made from copper containing less than  $0.1 \mu\text{Bq } ^{232}\text{Th}/\text{kg}$ . However, direct radiological measurements employing  $\sim 10 \text{ kg}$  of Cu measured for  $\sim 100$  days on the world's lowest background gamma-assay detectors have only resulted in limits on the  $^{232}\text{Th}$  chain at  $< 9 \mu\text{Bq}/\text{kg}$  [1]. In order to obtain assay sensitivity well below  $10 \mu\text{Bq}/\text{kg}$ , an inductively coupled-plasma/mass spectrometry (ICP-MS)-based assay was explored.

## Methods and Results

Several ion exchange resins were investigated to perform separation of the copper from thorium. The most promising technique utilized TRU resin to bind thorium from the copper samples. Samples were dissolved in concentrated nitric acid and spiked with a  $^{229}\text{Th}$  tracer. The resulting solution was then passed through a column packed with resin allowing the copper to elute through with virtually no retention. The bound thorium was then stripped from the column using oxalate and m/z 229 and 232 were measured using an APEX high-efficiency sample introduction system in combination with the ICP-MS.

Uncertainty estimates were obtained from a series of analysis runs employing seven identical columns loaded with TRU resin. After the initial reduction in background during the first three runs, presumably related to washing Th from the entire system, the quantity of thorium in the blanks levelled off to an average equivalent concentration of  $0.6 \mu\text{Bq Th/kg Cu}$  as shown in Table 3.

Table 3:  $^{232}\text{Th}$  normalized to  $\mu\text{Bq/kg Cu}$  from blanks using TRU resin

	Run 1	Run 2	Run 3	Run 4	Run 5	Run 6	Run 7	Ave 4-7
Column 1	67.2	10.4	2.0	0.7	0.7	1.7	1.1	1
Column 2	22.3	8.2	1.3	0.7	0.1	0.6	0.6	0.5
Column 3	26.6	7.8	1.7	0.5	0.6	0.6	0.5	0.6
Column 4	32.1	6.9	1.2	0.4	0.4	0.7	0.5	0.5
Column 5	36.0	7.8	1.5	0.5	0.3	0.6	0.7	0.5
Column 6	21.3	7.6	1.6	0.3	0.5	0.3	0.6	0.4
Column 7	34.5	6.2	2.1	0.8	0.4	0.5	0.6	0.6
Average	34.3	7.8	1.6	0.6	0.4	0.7	0.7	0.6
Std Dev	15.6	1.3	0.3	0.2	0.2	0.4	0.2	0.2
% RSD	45.5%	16.7%	20.6%	32.5%	46.1%	62.9%	30.0%	34.9%

After the blank analysis described above, two copper samples were analyzed. For each sample, a nominal 10 g of copper was dissolved in high purity nitric acid and seven aliquots of the resulting solutions were processed in a manner identical to the blank samples using the seven columns.

Table 4 shows the  $^{232}\text{Th}$  concentration results for these two samples, one of starting anode copper and the other electroformed copper. The sample results in Table 4 have not been blank corrected (the blank value has not been subtracted from the sample result). As these data indicate, a statistically meaningful difference between the blank and samples is observed, but the difference between the thorium concentrations in the two copper samples is not significant. Duplicate samples of the electrolyte were also analyzed and were found to contain 73.9 and 79.3  $\mu\text{Bq }^{232}\text{Th/L}$ .

Table 4:  $^{232}\text{Th}$  ( $\mu\text{Bq/kg Cu}$ ) in Cu samples using TRU resin sample preparation

	Blanks (Ave)	Starting Cu	Electroformed Cu
Column 1	1.0	1.7	1.6
Column 2	0.5	1.6	1.2
Column 3	0.6	1.4	0.9
Column 4	0.5	1.5	2.0
Column 5	0.5	1.8	1.5
Column 6	0.4	1.0	1.3
Column 7	0.6	1.3	0.9
Average	0.6	1.5	1.3
Std Dev	0.2	0.2	0.4
% RSD	35%	17%	30%

## Discussion and Conclusions

The relatively similar amounts of Th found in the starting anode and electroformed copper samples was unexpected as earlier work indicated that there is a considerable rejection factor for thorium during electro-deposition, i.e., thorium in the electroplating bath is excluded or “rejected” from the growing copper matrix, leading to a net purification of the copper from thorium [2]. According to rejection factors calculated previously, the starting anode copper should contain a thousand times more Th than the electroformed copper. It was hypothesized then that the Th concentration in the electroforming bath itself must be significantly higher than the starting anode copper. This was confirmed when the electrolyte thorium concentrations were indeed much higher than expected.

The high concentration of thorium in the bath solution could not be accounted for by build-up from dissolving anode copper. It is also unlikely that it could come from dust since the baths, pumps, filters and tubing are initially leached along with all of the bath materials repeatedly with successively more pure nitric acid and then rinsed with high purity water, then kept covered and purged with nitrogen. The levels observed would have required  $\sim 100$  mg of dust containing  $1 \mu\text{g/g}$  Th to deposit in the bath solution, considered very unlikely given the class 1,000 – 10,000 cleanroom status of the laboratory and the limited amount of time the baths are open to this environment. The remaining possibility is that the thorium is from the recrystallized copper sulfate used in the initial formulation of the baths.

Although some researchers purify  $\text{CuSO}_4$  crystals via repeated recrystallization, such a method is apparently not sufficient to produce  $\text{CuSO}_4$  of the necessary purity. Given the potential contamination of the recrystallized  $\text{CuSO}_4$  and the purity of the anode copper,  $\text{CuSO}_4$  is now generated directly from the anode copper by running a current through a bath filled with ultra-pure sulphuric acid, which yields thorium concentrations in the bath not much higher than that found in the anode copper. This method will hopefully allow us to avoid unexpectedly high

$^{232}\text{Th}$  levels in solution in the electroforming baths that may be a limiting factor in producing ultra-low background copper.

## 2.2 Radiometric Assay

### Introduction

In an effort to directly determine the quantities of  $^{232}\text{Th}$  and  $^{238}\text{U}$  in the anode copper, it was determined that a radioassay could prove useful if detection limits similar to or better than those obtained by Brodzinski [1] could be obtained. This would allow a broader spectrum search for contaminant species and could serve as a second method verification of the ICP/MS assay.

### 2.2.1 Methods and Results

A subsample of copper from stocks used as anode copper at PNNL was obtained. Approximately 22 kg of 1 inch copper slugs (99.995% Cu) manufactured by Outo Kumpu, which had been previously assayed by ICP/MS, were cleaned using PNNL methods [5,6]. A 4 liter LDPE Marinelli was acid leached and packed to contain as much of the copper nuggets as possible (figure 17). The nuggets were then removed from the Marinelli and double bagged in 6 mil LDPE. This material was shipped to Laboratori Nazionali del Gran Sasso in Italy for counting on the GeMPI2 detector.



Figure 17. 4 liter LDPE Marinelli packed with 1" copper slugs

Upon receipt of the materials it was noted that the copper slugs had worn small holes through the containment bags during shipment. To be certain the slugs were clean before counting, the copper was cleaned once again using an abbreviated process. Using leached polypropylene containers the slugs were first washed for ~30 seconds in approximately 1M high purity nitric acid followed by three sequential rinses in >18 M $\Omega$  deionized water and then dried under nitrogen. The slugs were then loaded into the Marinelli using leached HDPE tongs.

As of this writing the slugs were still being counted at Gran Sasso.

## 2.3 Nucleation and Growth Studies, other Assay Techniques

### 2.3.1 Introduction

As it has become increasingly difficult to further purify copper from the impurities of interest, a better understanding of the mechanisms of contaminant co-deposition has become paramount. Nucleation and growth processes during electro-deposition can play an important role in contaminant deposition, so these were investigated via the examination of electrodeposited copper by scanning electron microscopy (SEM) with electron backscatter diffraction (EBSD). The localization of contaminants in relation to the grain structure of the copper was also investigated using secondary ion mass spectrometry (SIMS). Samples were imaged both before and after thermal cycling to determine the extent of recrystallization, which can change the localization of contaminants. Contaminant localization on a much smaller scale was also examined via laser-ablation ICP-MS (LA-ICP-MS).

### Methods and Results

Copper samples were deposited onto stainless steel cylindrical cathodes from an electrolyte of 188 g/L  $\text{CuSO}_4 \cdot 5\text{H}_2\text{O}$  and 75 g/L  $\text{H}_2\text{SO}_4$  in  $>18$  M $\Omega$  resistivity ultra-pure water. Electro-deposition was carried out using a periodic pulse-reverse power supply with a waveform of 60 ms at +0.3 V, 7.5 ms at 0.0 V, 25 ms at -0.3 V, and 7.5 ms at 0.0 V. All samples were heated to 250 °C for at least 1 hour, then quenched in cold water in order to remove them from the cathodes.

For SEM and SIMS analysis, sample cross-sections were mounted in epoxy for metallographic polishing and given a series of successively finer-grit mechanical polishing steps using diamond grits with a final polish of colloidal silica. For LA-ICP-MS, electroplated copper samples were etched in 3%  $\text{H}_2\text{O}_2$ /1%  $\text{H}_2\text{SO}_4$ .

The samples were examined individually in a JEOL 840 SEM equipped with an Oxford Energy Dispersive Spectrometer (EDS) and an HKL Channel 5 Electron Backscatter Diffraction system (EBSD) for measuring the texture and grain orientation. The JEOL 840 was operated at 20 keV using a beam current of around  $10^{-7}$  amps. To investigate the grain structure of the copper samples, the SEM electron probe was scanned over finite region chosen to capture the variations in grain structure. At each pixel position, a diffraction pattern was captured and indexed to the face-centered cubic (fcc) copper structure, producing an orientation map of the entire region that showed the individual grains, their crystallographic orientation, and the nature and distribution of various interfaces within the mapped region.

For SIMS analysis, a Cameca IMS-4f SIMS equipped with a resistive anode encoder (RAE) position-sensitive ion imaging detector was used. Negative secondary ion spectral scans were conducted with a 10 kV  $\text{Cs}^+$  primary ion beam and the ion pulse counting detection system. Positive secondary ion spectral scans were conducted with a 12.5kV  $\text{O}_2^+$  primary ion beam and also ion pulse counting. Different analysis spots were chosen when using the  $\text{Cs}^+$  or  $\text{O}_2^+$  primary ion beams. A  $\sim 500 \mu\text{m}^2$  area of each sample was presputtered for up to an hour to remove surface contamination. The mass spectrum was scanned in a presputtered sampling area, and then ion images were collected.

For LA-ICP-MS, an UP-266 Macro Laser (New Wave) coupled to a PQ-Excell ICP-MS (Thermo Elemental) was operated at 10 Hz and each 80  $\mu\text{m}$  spot was ablated for 5 seconds, with a delay of 10 seconds between spots. The laser was rastered across the copper surface to give spatial information.  $\text{M}/z$  63 and 103 were monitored to indicate the relative abundance of the copper matrix reaching the ICP-MS and  $\text{m}/z$  232 and 238 were scanned to indicate Th and U contamination, respectively.

All of the samples showed a very fine grain size at the interior surface directly in contact with the mandrel. After a few hundred microns, this tended to transition to a larger elongated grain structure that often had a strong texture (Figure 18). For some samples, the texture continued to refine itself out to the edge of the sample, producing very large, highly oriented grains (Figure 19). Comparison of SEM images of the copper samples before and after thermal cycling indicated that the copper recrystallizes considerably during thermal cycling (Figure 20), with smaller, more randomly oriented grains merging to form larger grains with a more consistent crystal orientation.

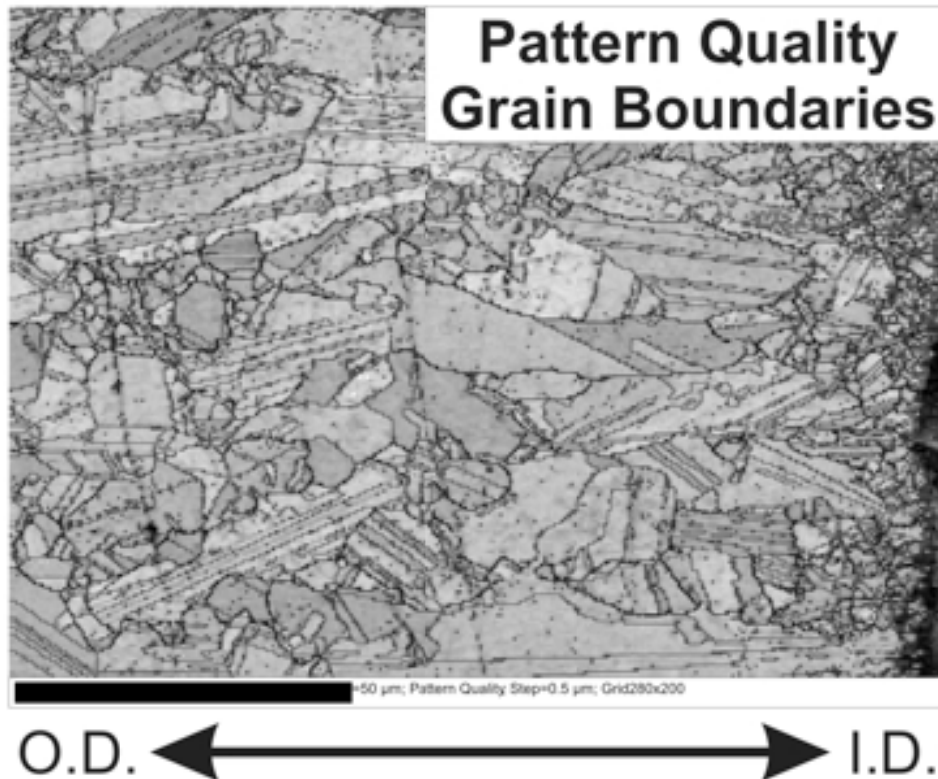


Figure 18: EBSD map from the inside diameter location of sample #1 showing the transition from a very fine grained region to much larger, highly orientated and elongated grain structure. The black bar in the figure represents 50  $\mu\text{m}$ .

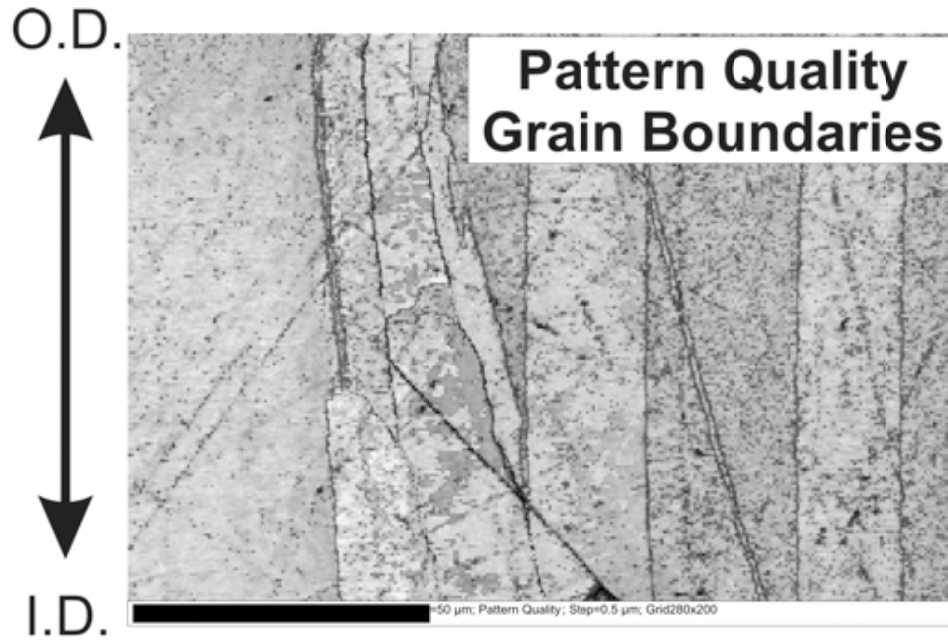


Figure 19: EBSD map showing a highly elongated and oriented grain structure near the outer diameter region of sample #7. The black bar in the figure represents 50  $\mu\text{m}$ .

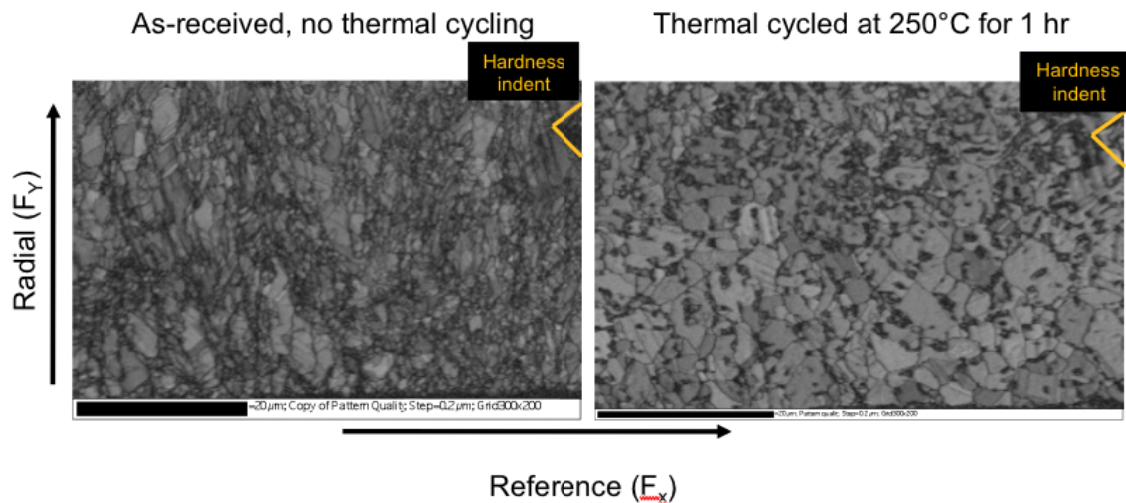


Figure 20: Comparison of SEM pattern quality before and after thermal cycling. Images were taken at the same location on the sample.

The SIMS negative ion spectra indicated S and Cl were significant impurities (Figure 21). The level of O in the negative ion scan indicates a relatively low level of O in the Cu samples. Impurity elements indicated in the positive ion spectra include mainly Na, Al, K, and Ca (Figure 22). Most or all of the O ion signal in the positive ion scan is from the primary ion beam, rather than the sample matrix. Th and U were below detection limits.

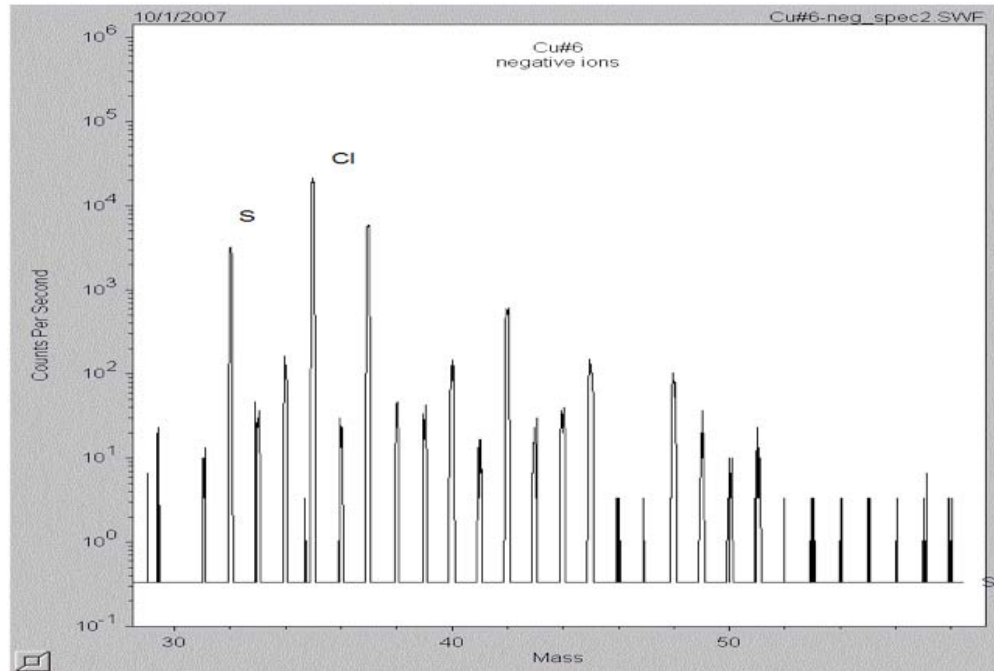


Figure 21: Representative SIMS negative ion spectra showing S and Cl impurities.

The ion images indicate both S and Cl occurred in very small (< 5-10 microns) inclusions (Figure 23). The small sizes of the inclusions were also indicated by the observation that they appeared and disappeared in as little as a few seconds in real time, as layers of the sample were gradually removed by the SIMS primary ion beam. Ion images for Cl also show enhanced incorporation at the start of deposition during nucleation (Figure 24). The co-localization of the S- and Cl-bearing inclusions is indicated in Figures 23 and 25.

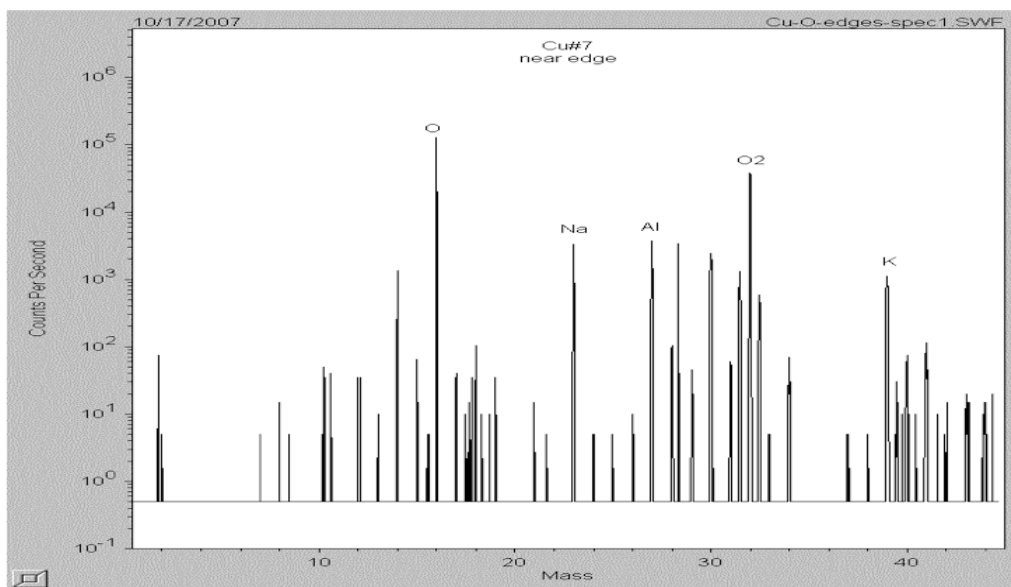


Figure 22: Representative SIMS positive ion spectra showing Na, Al, and K impurities.

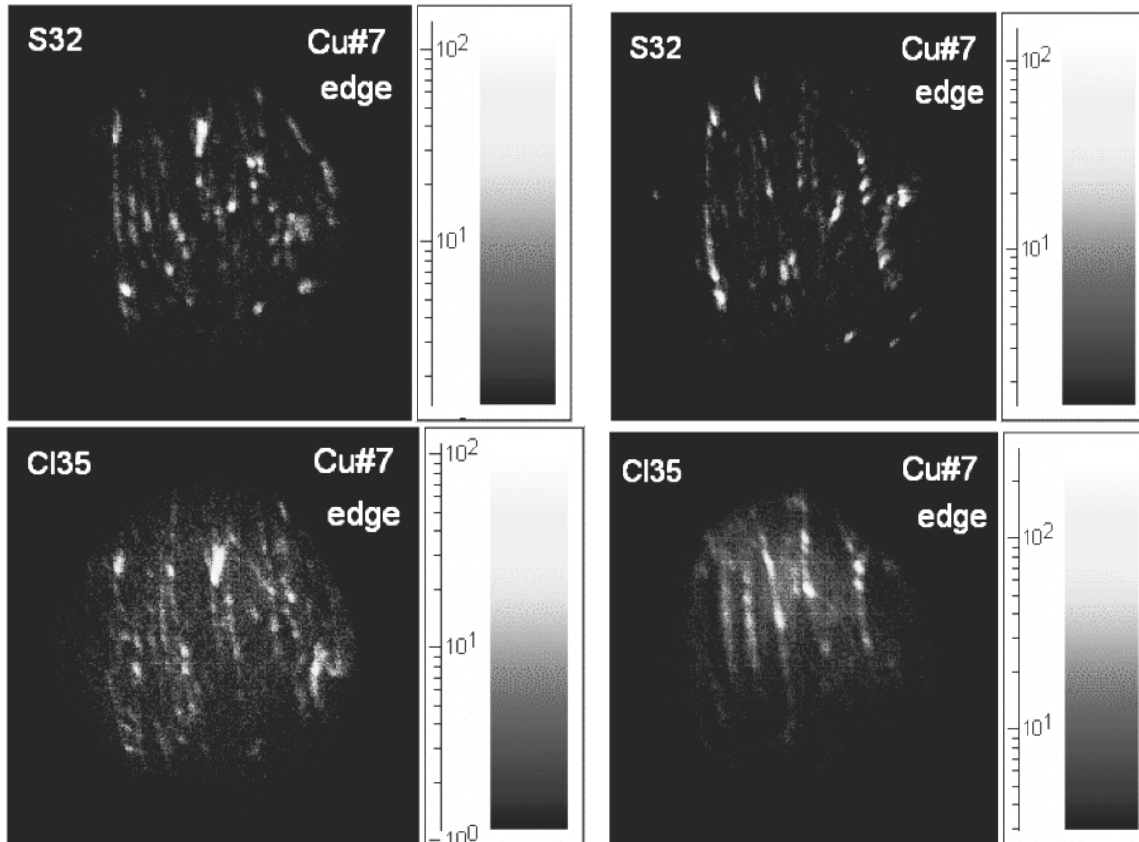


Figure 23: Series of SIMS ion images showing the localization of sulfur and chlorine contaminants. The spot size for these images is 150  $\mu\text{m}$ .

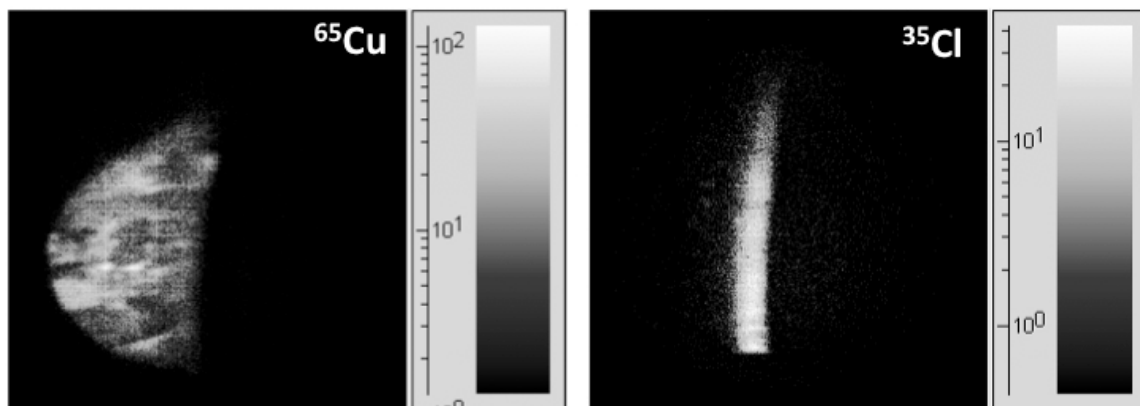


Figure 24: SIMS images at the mandrel showing enhanced chlorine incorporation during nucleation.

The laser ablation data indicated very low levels of thorium and uranium in the copper samples. They also appeared to co-deposit in inclusions (Figure 26).

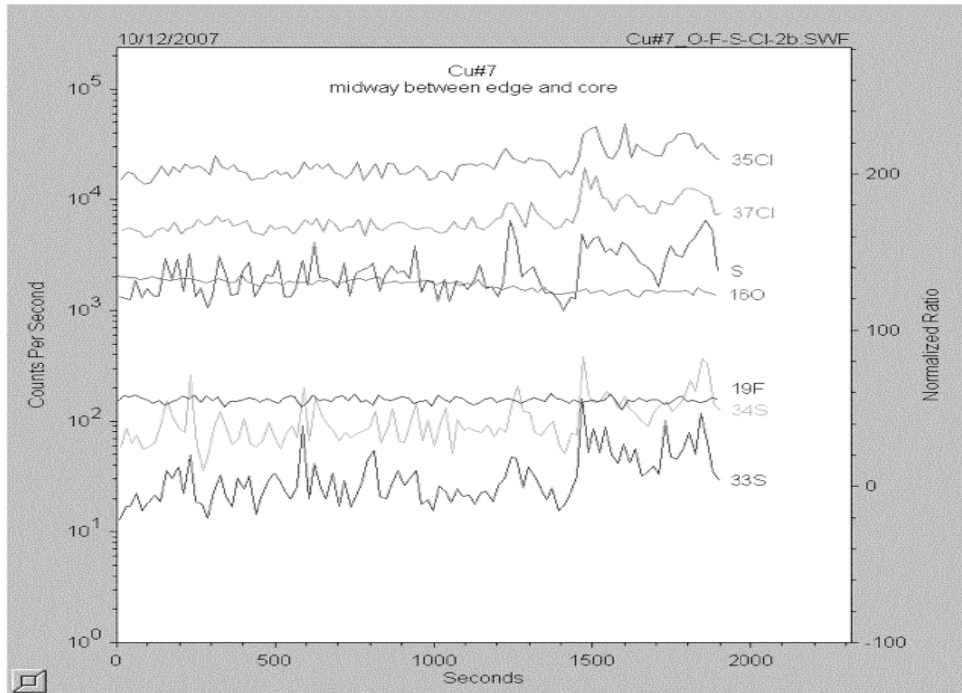


Figure 25: SIMS ion count rates versus time in a single spot showing co-localization of sulfur and chlorine.

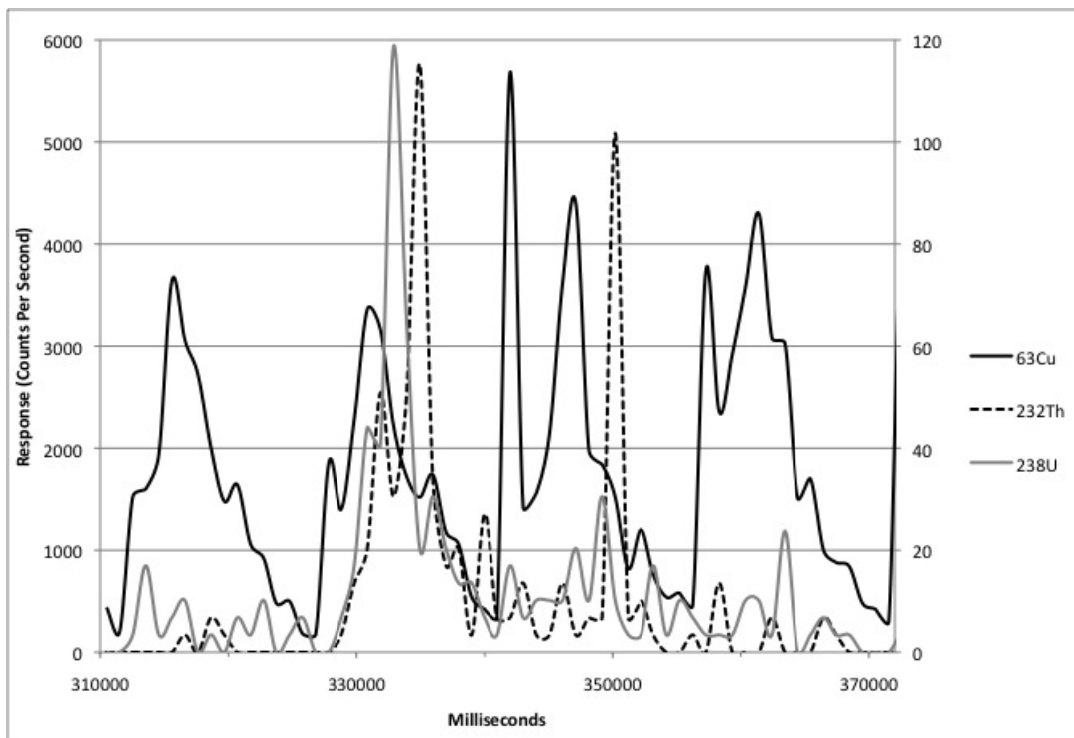


Figure 26: LA-ICP-MS trace showing co-localization of Th and U contaminants. The response for Cu is plotted on the primary y-axis and the response for Th and U is on the secondary y-axis. Each Cu peak represents an 80  $\mu\text{m}$  spot.

## Discussion and Conclusions

SEM imaging of the copper samples shows many fine, uniformly sized grains directly next to the cathode, indicating that nucleation may be instantaneous. Periodic pulse-reverse electroplating may facilitate this, as the reverse pulse limits grain growth. The high density of nucleation sites may favor increased impurity incorporation into the first few layers of copper. The large, highly textured grains seen in the middle and outer regions are likely the result of recrystallization during thermal cycling. The physical properties of the copper may be more influenced by this transition than by the as-deposited grain structure.

The overall pattern for the S and Cl isotopes in the SIMS data suggests that S and Cl are co-located in inclusions. Furthermore, the ion images show that the S and Cl inclusions are highly oriented and appear to align with the grain boundaries shown in the EBSD pattern quality map for that sample (Figures 19 and 23). Laser ablation of electroformed copper indicates that Th and U may be present in inclusions in the copper matrix, consistent with the SIMS results for other contaminants.

This data provides evidence for instantaneous nucleation and highly selective grain growth during the electro-deposition process, though further work needs to be done in order to distinguish between nucleation and growth patterns and the effects of self-annealing or recrystallization. Both SIMS and laser ablation show non-homogeneous distribution of various contaminants, indicating, again, that co-deposition of these impurities is more a function of surface absorption and encapsulation during grain growth than redox chemistry. Finding trace metallic impurities in the copper, especially those with radioactive isotopes such as potassium, indicates that further precautions need to be taken to prevent bath contamination and also that the mechanisms of contaminant deposition should be thoroughly understood so that process parameters can be modified to prevent the incorporation of impurities.

## 2.4 Conclusions

As copper of increasing purity is produced, assay limits have been pushed lower, necessitating the concurrent development of improved assay methods. At the same time, it has become increasingly difficult to further purify copper from the impurities of interest, so efforts have also been focused on understanding the mechanisms of contaminant co-deposition. To help achieve our purity goals, an ICP-MS-based method for assay of thorium in ultra-pure copper has been developed. Based on these latest data, both the detection limits of the ICP-MS assay and the copper being produced are still 3-4 times too high thorium in order to meet the purity goals of Majorana for thorium.

Copper nucleation and growth were studied using SEM and SIMS. Samples were imaged both before and after thermal cycling to determine the extent of recrystallization, which can change the localization of contaminants. Contaminant localization on a much smaller scale was also examined via SIMS and LA-ICP-MS. The SIMS analysis did not prove adequately sensitive to locate Th or U. LA-ICP-MS provided adequate sensitivity so may be useful as a surface screening tool but the data was difficult to interpret, was inconsistent in its performance, and would prove very difficult to develop into a quantitative assay.

A portable clean room was purchased to provide a clean environment for experiments involving very low levels of thorium and uranium. This should help to lower method detection limits for the ICP-MS assay. In addition, a multi-channel electro-analytical potentiostat was acquired to elucidate the electrochemical mechanisms at play during electro-deposition.

### 3.0 References

- [1] R.L. Brodzinski, et al. 1995. *J. Radioanal. Nucl. Chem.* 193(1): 61-70.
- [2] E.W. Hoppe, et al. 2008. *J. Radioanal. Nucl. Chem.* 277 (1): 103-110.
- [3] E.W. Hoppe, et al. 2009. *J. Radioanal. Nucl. Chem.* DOI 10.1007/s10967-009-0241-1
- [4] E.W. Hoppe, et al. 2009. Submitted to Nuclear Inst. and Methods in Physics Research, A. Ref No. NIMA-D-09-00453. *Further Reductions of Radioactive Backgrounds in Electroformed Copper for Ultra-Sensitive Radiation Detector.*
- [5] E.W. Hoppe, et al. 2008. *J. Radioanal. Nucl. Chem.* 276(3):645-650. doi:10.1007/s10967-008-0612-z
- [6] E.W. Hoppe, et al. 2007. *Nucl. Instru. and Meth. in Physics Res. Sec A.*, 579(1):486-489. doi:doi:10.1016/j.nima.2007.04.101



**Pacific Northwest**  
NATIONAL LABORATORY

902 Battelle Boulevard  
P.O. Box 999  
Richland, WA 99352  
1-888-375-PNNL (7665)  
[www.pnl.gov](http://www.pnl.gov)



U.S. DEPARTMENT OF  
**ENERGY**